Frontiers in Heat and Mass Transfer

Tech Science Press

https://doi.org/10.32604/fhmt.2026.080306

ARTICLE

Optimization Study on Operating Parameters of Rotary Gas-Gas Heat Exchanger in Low- and Medium-Temperature Denitrification System for Cement Kiln Flue Gas

Kaiwen Cheng[1], Yi Sun[2], Dong Wang[3,*], Chen Zhu[2] and Fuping Qian[2,*]

[1]School of Civil Engineering and Architecture, Ma'anshan University, Ma'anshan, China
[2]School of Energy and Environment, Anhui University of Technology, Ma'anshan, China
[3]School of Civil Engineering and Architecture, Anhui University of Technology, Ma'anshan, China

*Corresponding Authors: Dong Wang. Email: wangdong224545@163.com; Fuping Qian. Email: fpingqian@ahut.edu.cn

Received: 06 February 2026; Accepted: 08 May 2026; Published: 29 June 2026

ABSTRACT: Rotary gas-gas heat exchangers (GGHs) are pivotal for waste heat recovery in low- and medium-temperature denitrification systems of cement kilns. This study examines the performance of GGHs within such systems by coupling computational fluid dynamics (CFD) with the response surface method (RSM), introducing overall system performance (OSP) as the principal optimization criterion. The investigation systematically elucidates the effects of treated flue gas inlet temperature, inlet velocity, and rotor speed on GGH efficiency. Findings reveal that OSP increases with rotor speed but reaches a plateau beyond 1 rpm; it decreases with higher inlet velocity and increases with higher inlet temperature. Response surface analysis identifies treated flue gas inlet temperature as the most influential parameter, highlighting a synergistic effect between rotor speed and inlet temperature, alongside an antagonistic interaction between inlet temperature and inlet velocity. To ensure safe system operation, engineering constraints were incorporated into the optimization framework using a Box-Behnken design. The optimal operational parameters were determined as a treated flue gas inlet temperature of 250°C, inlet velocity of 8 m/s, and rotor speed of 1 rpm, yielding a maximum OSP of 107.74. The integrated CFD-RSM methodology and constraint-aware optimization strategy presented in this study offer a practical reference for enhancing the operational efficiency of industrial waste heat recovery systems, particularly in cement kiln SCR applications.

KEYWORDS: Waste heat recovery of cement kiln; rotary gas-gas heat exchanger; response surface method; operating parameter optimization

1 Introduction

Cement production is a cornerstone of China's national economic development, yet it remains a high-energy-consumption industry with considerable potential for energy conservation and carbon emission reduction. China has sustained the world's largest cement output for several consecutive years [1–3]. In response to climate change and environmental pollution, the Chinese government has enacted a series of stringent policies, including the "Action Plan for Carbon Peaking by 2030" [4] and the "Opinions on Promoting Ultra-Low Emissions in the Cement Industry" [5], which require cement kilns and waste heat recovery systems to achieve ultra-low emissions of particulate matter, sulfur dioxide, and nitrogen oxides. Consequently, the deployment of selective catalytic reduction (SCR) denitrification systems has become indispensable in modern cement production [6].

In low- and medium-temperature SCR denitrification systems for cement kilns, the rotary gas-gas heat exchanger (GGH) serves a pivotal role in waste heat recovery. As a compact and highly efficient heat exchange device, the rotary GGH captures thermal energy from the high-temperature flue gas exiting the SCR reactor and transfers it to preheat the lower-temperature incoming flue gas, thereby significantly reducing the energy required for reheating. Its operating principle involves a rotor equipped with heat exchange elements that rotate continuously, allowing these elements to alternately pass through hot and cold flue gas channels and facilitating periodic heat storage and release. The performance of the rotary GGH is influenced not only by the geometry of the heat exchange elements but also by key operational parameters [7,8].

Extensive research has been conducted on rotary heat exchangers. Dallaire et al. developed a finite-volume model that simplifies the GGH core as a porous medium and compared thermal equilibrium and non-equilibrium approaches [9]. Alhusseny and Turan demonstrated that the porous medium approximation effectively captures the flow and heat transfer behavior in rotary regenerators [10]. Güllüce and Özdemir constructed a comprehensive CFD model of a rotary GGH in a desulfurization system and validated its predictions against analytical solutions [11]. Due to the substantial temperature difference between the solid matrix and the gas phase, the local thermal non-equilibrium (LTNE) model has become the preferred framework in rotary GGH simulations.

Optimization of operating parameters represents another critical research direction. Ghodsipour and Sadrameli [12] applied an orthogonal experimental design to examine the effects of rotational speed and gas temperature on rotary air preheater performance. Güllüce and Özdemir [11] conducted a comprehensive optimization of rotary GGHs in desulfurization systems, considering efficiency, entropy generation, and cost as objective functions. More recently, studies have successfully integrated response surface methodology (RSM) with CFD for the heat exchanger optimization. Wang and Han [13] developed a hierarchical optimization framework for aluminum slotted finned tube heat exchangers, combining orthogonal screening, analysis of variance, and RSM, and achieved notable improvements in overall performance. Consequently, RSM has emerged as a robust statistical tool for heat exchanger optimization, enabling the efficient exploration of multi-parameter design spaces with minimal experimental or computational efforts.

Despite these advances, several research gaps persist. First, existing studies have largely concentrated on applications in coal-fired power plants, with comparatively limited attention given to the distinctive characteristics of flue gas systems in cement kilns. In such systems, SCR processes typically follow a “dust removal followed by denitrification” sequence, leading to flue gas conditions at the GGH inlet that differ substantially from those observed in coal-fired facilities [14–16]. Second, while analyses of individual operating parameters are common, investigations into the coupled effects and interactions among multiple parameters remain insufficient. For example, most optimization studies prioritize heat transfer efficiency, often neglecting the inherent trade-off between heat transfer enhancement and pumping power consumption. In addition, engineering safety constraints are frequently introduced as post-optimization screening criteria rather than being intrinsically integrated into the optimization framework. Although CFD-RSM coupling has been employed in the optimization of various heat exchangers, its application to rotary GGHs in cement kiln SCR systems, characterized by distinct flue gas conditions and stringent safety requirements, remains largely unexplored [17,18].

This study proposes a practical approach that embeds engineering safety constraints directly within a response surface optimization framework, focusing on application-oriented parameter optimization. Variable levels are defined using a Box-Behnken design, through which the SCR catalyst’s active temperature window and the conventional flue gas flow rate range are incorporated into the optimization model, ensuring that all test points remain within the safe operating region. The rotational speed range is determined through preliminary CFD screening, identifying the critical threshold beyond which performance gains associated with increased rotational speed begin to plateau. This constraint-embedding strategy differs fundamentally

from post-optimization screening, ensuring that the resulting optimal parameters are inherently safe and practical from an engineering perspective. Moreover, the methodology is readily extendable to the optimization of other industrial systems beyond the scope of this study's specific application [19].

In summary, this study focuses on the rotary GGH within low- and medium-temperature denitrification systems for cement kiln flue gas. Three operational parameters commonly encountered in engineering practice—inlet flue gas velocity, flue gas temperature, and rotary GGH rotor speed—were selected as the primary study factors. The overall system performance (OSP) indicator, which balances heat transfer capacity against pumping power consumption, is adopted as the response variable. On this basis, CFD coupled with RSM is employed to systematically evaluate the influence of GGH operating parameters on the overall performance of the denitrification system. The objective is to enhance the recovery of high-temperature waste heat from the production process while minimizing the energy consumption associated with flue gas reheating.

2 Establishment of Computational Model

2.1 Physical Model

Based on the low- and medium-temperature denitrification system of cement kilns, a geometric model of a rotary GGH is established, comprising the inlet and outlet flues for both treated and untreated flue gases, the rotor, and the sealed region separating the two gas streams. The two flue gases pass through the rotor in opposite directions. The geometric model, constructed according to the parameters listed in Table 1, is presented in Fig. 1.

Table 1: Geometric parameters of rotary GGH in a cement kiln.

Geometric Parameters	Value
Outer diameter of rotor D_w/mm	5400
Shaft diameter of rotor D_Z/mm	1120
Rotor height Z/mm	1020
Share of untreated flue gas side/%	45
Share of treated flue gas side/%	45
Share of sealed area/%	10
Porosity γ	0.836
Specific surface area/m^2/m^3	501.522

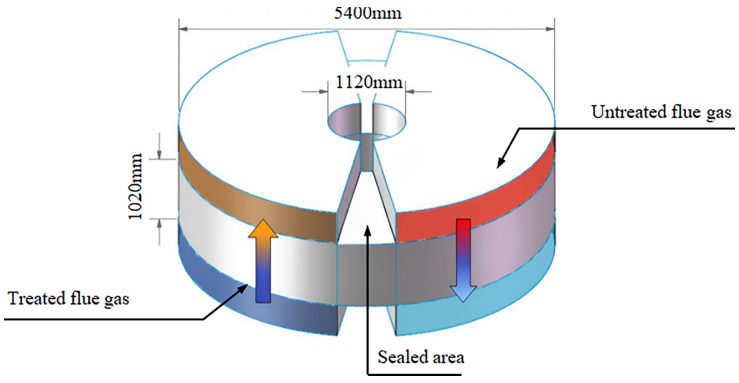

Figure 1: Geometric structure of rotary GGH.

2.2 Porous Media Heat Transfer Model

The compartments of a rotary GGH rotor consist of a large number of densely packed heat transfer elements arranged in parallel, thereby dividing the rotor into multiple microchannels of identical structure—a configuration consistent with the characteristics of a porous medium [20]. Based on this simplification, the corresponding mathematical model has been used to simulate heat and mass transfer processes within the rotary heat exchanger, with the results validated against experimental data, demonstrating that the porous medium model provides reliable predictions [21]. Considering the actual flow and heat transfer conditions within the rotary GGH rotor, this study adopts a local thermal non-equilibrium (LTNE) porous medium model for simulation. In Fluent, the LTNE model is implemented using a two-energy-equation approach, in which separate energy equations are solved for solid and fluid phases and subsequently coupled [22,23]. The governing energy equations for LTNE in a porous medium are as follows.

The energy equation for the fluid phase is expressed as follows:

$$\gamma c_{\mathrm{pf}} \frac{\partial \left(\rho_{\mathrm{f}} T_{\mathrm{f}}\right)}{\partial t} + \nabla \cdot \left(\rho_{\mathrm{f}} u_{\mathrm{f}} h_{\mathrm{f}}\right) = \nabla \cdot \left(k_{\mathrm{f,eff}} \nabla T_{\mathrm{f}}\right) + h_{\mathrm{sf}} \alpha \left(T_{\mathrm{s}} - T_{\mathrm{f}}\right) \tag{1}$$

The energy equation for the solid phase is expressed as follows:

$$(1-\gamma) \rho_{\mathrm{s}} c_{\mathrm{s}} \frac{\partial T_{\mathrm{s}}}{\partial t} = \nabla \cdot \left(k_{\mathrm{s,eff}} \nabla T_{\mathrm{s}}\right) - h_{\mathrm{sf}} \alpha \left(T_{\mathrm{s}} - T_{\mathrm{f}}\right) \tag{2}$$

In the equation, γ denotes the porosity of the porous medium region, $k_{\mathrm{f,eff}}$ and $k_{\mathrm{s,eff}}$ represent the effective thermal conductivities of the fluid and solid phases, respectively (W/(m·K)), α is the specific surface area of the porous medium region, expressed in $\mathrm{m^2/m^3}$, u_{f} denotes the fluid velocity (m/s), h_{sf} represents the interfacial heat transfer coefficient between the fluid and solid ($\mathrm{W/m^2 \cdot k}$), T_{f} and T_{s} are the temperatures of the fluid and solid phases, respectively (K), c_{pf} and c_{s} are the specific heat capacities of the fluid and solid, respectively, (J/(kg·K)), and ρ_{f} and ρ_{s} represent the densities of the fluid and solid, respectively ($\mathrm{kg/m^3}$).

2.3 Rotating Model

Fluent offers several simulation approaches for modeling moving and rotating flow processes within the entire computational domain or selected subdomains. Considering the operational characteristics of the rotary GGH, the Moving Reference Frame (MRF) model was used to simulate its rotational pattern, with a stationary coordinate system assigned to the flue gas flow region and a rotating coordinate system applied to the solid matrix region. The MRF model is well-suited for steady-state flow simulations and provides high accuracy when the relative motion of grid boundary points is nearly uniform [24]. The velocity within the rotating domain is computed as described in Eq. (3).

$$v_r = v - \left(v_{\mathrm{t}} + \omega \times r\right) \tag{3}$$

In the equation, v represents the absolute velocity in the inertial coordinate system, v_{r} denotes the relative velocity in the rotating coordinate system, v_{t} is the translational velocity of the rotating region, all expressed in m/s, and ω is the angular velocity, in rad/s.

2.4 Physical Properties and Boundary Conditions

As shown in the process flow of the low- and medium-temperature denitrification system, the flue gas undergoes desulfurization and dust removal before entering the rotary GGH. Therefore, it can be assumed that the flue gas is free of sulfides and particulates, with a low concentration of nitrogen oxides [25]. Under

these conditions, the flue gas is modeled as an ideal gas mixture, with its density, specific heat capacity, dynamic viscosity, and thermal conductivity expressed as temperature-dependent functions. In FLUENT, a piecewise-linear interpolation method is employed to compute these properties, enabling real-time updates of the physical parameters as the temperature varies. The relevant physical properties are summarized in Table 2.

Table 2: Physical properties of standard flue gas under normal atmospheric pressure.

Temperature T/K	Density ρ/(kg/m^3)	Specific Heat Capacity C_p/[J/(kg·K)]	Dynamic Viscosity $\mu \times 10^5$/Pa·s	Thermal Conductivity $\lambda \times 10^2$/[W/(m·K)]
273	1.295	1042	1.58	2.28
363	0.985	1065	1.994	3.045
373	0.950	1068	2.04	3.13
423	0.849	1083	2.245	3.57
473	0.748	1097	2.45	4.01
488	0.7285	1100.9	2.5055	4.1345
523	0.683	1110	2.635	4.425
573	0.617	1122	2.82	4.84

At the computational domain inlet, a velocity boundary condition is imposed, while a pressure outlet boundary condition is applied at the outlet. All flue walls, outer rotor walls, rotor shaft walls, and seal chamber walls of the rotary GGH are treated as adiabatic boundaries, with standard wall functions implemented to capture near-wall turbulence effects. The Realizable k-ε turbulence model is employed to simulate turbulent flow, and the SIMPLE algorithm is used to couple pressure and velocity fields. Convection terms in the governing equations are discretized using a second-order upwind scheme [26–28], ensuring higher-order accuracy in the transport calculation. Convergence is evaluated using residual criteria of 10^{-4} for the continuity and momentum equations and 10^{-6} for the energy equation. In addition, outlet average temperature and pressure drop are continuously monitored. Convergence is considered achieved only when the relative variations of these quantities remain below 0.1% for 500 consecutive iterations, providing an auxiliary check to complement the residual-based criterion.

It should be noted that the numerical simulations in this study assume a dust-free flue gas and neglect ammonium bisulfate (ABS) deposition. These assumptions are justified for the low-temperature denitrification system examined here, which is located downstream of the baghouse filter, has undergone desulfurization treatment, and operates with well-controlled SCR ammonia slip. When extending this methodology to other plants or operating conditions, the potential impact of high flue gas dust concentrations and ABS deposition on flow resistance and heat transfer performance must be carefully considered. If necessary, multiphase flow or deposition models should be incorporated to capture these effects accurately.

2.5 Mesh Generation

Structured grids provide rapid generation and high mesh quality, as all interior points have adjacent cells in the six principal coordinate directions, except at boundaries. However, their application becomes challenging for geometries with complex features. Typically, structured grids employ parameterization or spline interpolation to fit surfaces and volumes, allowing for accurate representation of boundaries. As a result, the generated mesh is smoother and better aligned with the actual geometry. Furthermore, structured grids simplify data preparation and parameter assignment, while offering improved computational stability

and faster convergence. Considering the relatively regular overall geometry of the rotary GGH, structured grids are selected for its mesh generation [29].

In CFD simulations, flow characteristics are inherently determined by the computational grid, meaning that variations in grid resolutions can significantly affect the results. Coarse grids may fail to capture critical flow details, whereas excessively fine grids increase computational cost and can introduce numerical dissipation errors. Consequently, verification of grid independence is essential for the computational model. The results of the grid sensitivity analysis are shown in Fig. 2.

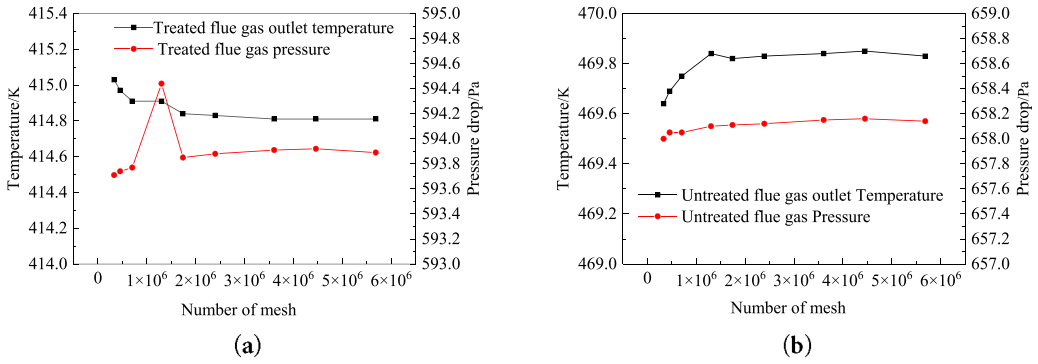

Figure 2: Pressure drop at the inlet and outlet of flue gas and outlet temperature values under different grid numbers: (**a**) Treated flue gas side; (**b**) Untreated flue gas side.

The grid sensitivity analysis indicates that the computational results fluctuate when the total number of grid cells is below 2 million. Once the grid account reaches 2.39 million, the pressure drops and outlet temperatures for the untreated and treated flue gas streams stabilize, exhibiting negligible variation. Consequently, this grid density provides an optimal compromise between computational accuracy and efficiency. The final computational grid model is shown in Fig. 3.

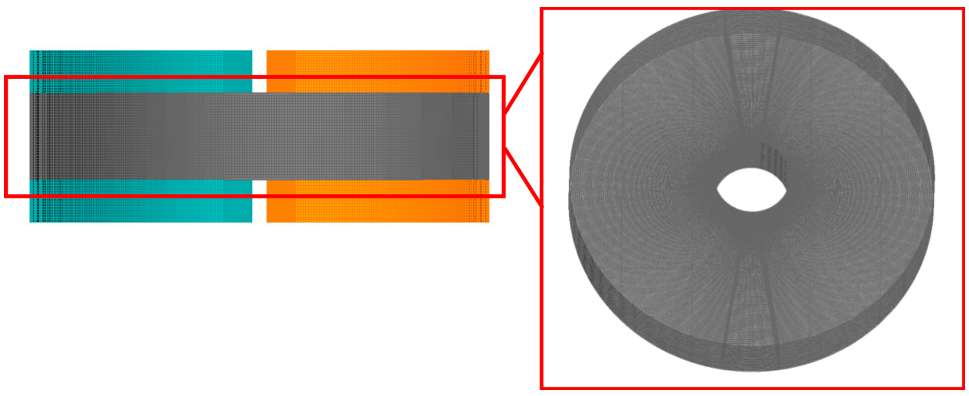

Figure 3: Schematic diagram of grid structure.

2.6 Model Validation

To assess the feasibility of simulating a rotary GGH using a porous-medium LTNE model coupled with a multiple reference frame (MRF) approach, a geometric model was constructed based on the rotary GGH parameters reported in Reference [30], as shown in Fig. 4. The simulation was performed under the operating conditions and with the porous-medium parameters provided in the reference study.

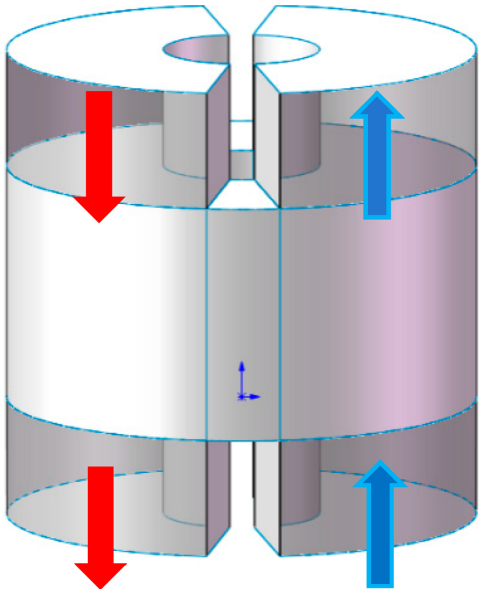

Figure 4: Schematic diagram of a rotating GGH computational model.

The simulation results are summarized in Table 3. Deviations from the analytical solutions reported in the literature are less than 5%, which is within an acceptable range. These findings confirm that the porous medium LTNE model coupled with the MRF approach is suitable for subsequent simulation analysis of the rotary GGH. It should be emphasized that the validation is conducted against analytical solutions from literature, and no experimental or plant-scale data is available for further verification.

Table 3: CFD results and validation under design conditions.

Comparison Item	CFD Results	Analytical Solutions	Relative Error (%)
Untreated high-temperature flue gas outlet temperature (°C)	69.97	71.64	2.33
Treated low-temperature flue gas outlet temperature (°C)	99.73	98.69	1.05
Heat transfer efficiency	0.6654	0.6503	2.322

3 Optimization Design Scheme for Rotary GGH Operating Conditions Using Response Surface Methodology

3.1 Operating Parameter Setting

The rotary GGH examined in this study is employed in low- and medium-temperature denitrification systems. The flue gas parameters entering the rotary GGH must meet the requirements for stable overall system operation. The inlet conditions of the untreated flue gas correspond to the outlet of the bag filter, with the inlet temperature exhibiting a relatively narrow variation range. In contrast, the treated flue gas enters from the outlet duct of the SCR reactor, which operates within a broader temperature range of 180°C–250°C. As a result, variations in the inlet conditions of the treated flue gas have a greater impact on rotary GGH performance than those of the untreated flue gas [31]. The inlet velocity is limited to the conventional design range of 8–12 m/s for cement kiln flue gas systems, as velocities below 8 m/s may cause ash deposition in ducts, whereas velocities above 12 m/s increase erosion risk and system resistance. To ensure that all

parameters remain within the system's safe operating envelope, a Box-Behnken design was employed, with treated flue gas inlet temperature, inlet velocity, and rotary GGH rotational speed selected as the three factors for response surface analysis.

Although the inlet temperature and velocity of the flue gas are constrained by actual operating conditions, the rotary GGH rotational speed requires preliminary screening. As shown in Fig. 5, the pressure drop and outlet temperatures of both the untreated and treated flue gas streams vary with rotational speed.

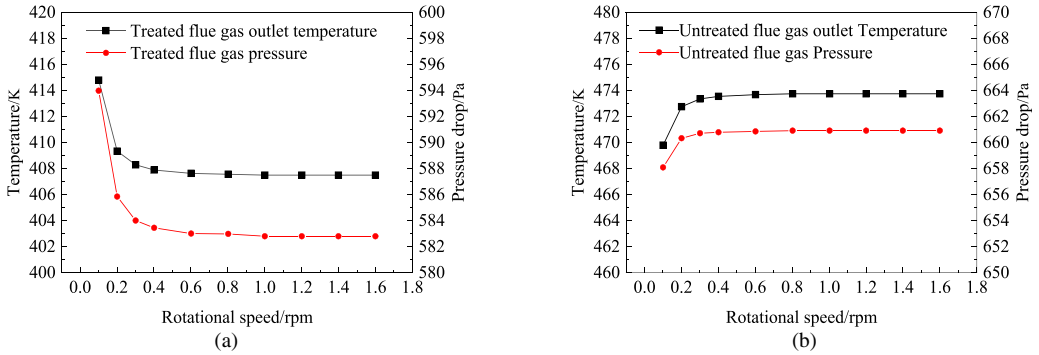

Figure 5: Pressure drops and outlet temperatures of flue gases at different rotational speeds: (**a**) Treated flue gas; (**b**) Untreated flue gas.

As the rotational speed increases, the outlet temperature and pressure drop of the untreated flue gas increase, whereas those of the treated flue gas decrease steadily. When the rotational speed approaches approximately 1 rpm, the pressure drop and outlet temperature for both gas streams begin to stabilize. This behavior indicates that further increases beyond 1 have only a minor effect on the overall performance of the rotary GGH. Therefore, the operational rotational speed range is defined as 0.1 to 1 rpm.

It should be emphasized that the parameter settings cited above are specific to the cement kiln denitrification system examined in this study. When applying these results to other facilities or process conditions, the suitability of these parameters must be carefully evaluated in the context of the actual operating conditions.

3.2 Evaluation Metric

Since the flue gas is dedusted by the bag filter before entering the rotary GGH, it is assumed to be dust-free, and ash deposition within the rotary GGH is neglected. The primary deposit typically observed in rotary GGHs is ammonium bisulfate (ABS), formed from the reaction of SO_3 and NH_3 escaping the SCR unit. In this low- and medium-temperature SCR denitrification system, the flue gas has undergone desulfurization treatment, rendering the effect of ABS deposition negligible. Consequently, this study focuses solely on the heat transfer and flow resistance characteristics of the rotary GGH. The following evaluation indicators are selected to assess rotary GGH performance [32].

The heat transfer effectiveness of the low-temperature and high-temperature flue gas streams is defined by Eqs. (4) and (5).

$$\varepsilon_c = \frac{Q_c}{Q_{max,c}} = \frac{m_c\left(c_{pco}T_{co} - c_{pci}T_{ci}\right)}{m_c\left(c_{phi}T_{hi} - c_{pci}T_{ci}\right)} \tag{4}$$

$$\varepsilon_h = \frac{Q_h}{Q_{max,h}} = \frac{m_h\left(c_{phi}T_{hi} - c_{pho}T_{ho}\right)}{m_h\left(c_{phi}T_{hi} - c_{pci}T_{ci}\right)} \tag{5}$$

In the equation, the following notation is used: c—cold fluid (treated flue gas); h—hot fluid (untreated flue gas); I—inlet; o—outlet. The heat exchange effectiveness of the low- and high-temperature flue gases is denoted by ε_c and ε_h, respectively. Q_c and Q_h represent their respective heat transfer rates (kW), while $Q_{max,c}$ and $Q_{max,h}$ correspond to the maximum achievable heat transfer rates (kW). The specific heat capacities of the low-temperature flue gas at the inlet and outlet are c_{pci} and c_{pco} (J/(kg·K)), and those of high-temperature flue gas are c_{phi} and c_{pho} (J/(kg·K)). T_{ci} and T_{co} denote the inlet and outlet temperatures of the low-temperature flue gas (K), while T_{hi} and T_{ho} represent the corresponding temperatures of the high-temperature flue gas (K).

The system's pumping power (PP_t) is defined by Eq. (6).

$$PP_t = PP_c + PP_h = \frac{m_c}{\rho_c}\Delta P_c + \frac{m_h}{\rho_h}\Delta P_h \tag{6}$$

In the equation, PP_c and PP_h denote the pumping powers of the low- and high-temperature flue gases (kW), respectively. m_c and m_h represent their respective mass flow rates (kg/s) while ρ_c and ρ_h indicate their densities (kg/m^3); ΔP_c and ΔP_h correspond to the pressure drops of the low- and high-temperature flue gases (Pa), respectively.

To balance heat transfer efficiency and energy consumption in practical engineering applications, an OSP index that integrates these two evaluation criteria is employed, as defined below.

$$OSP = 0.5\left(Q_c + Q_h\right)/PP_t \tag{7}$$

The OSP is defined as the ratio of the total heat transfer rate recovered by the system to the total pumping power consumed. This dimensionless index serves as an engineering indicator for evaluating the energy utilization efficiency of rotary GGHs. Previous studies have employed similar performance matrices, including the "ratio of heat transfer to pump power consumption (Q/N)", "heat transfer rate per unit pump power", "energy utilization index", and "transition performance evaluation criteria", all of which share the same underlying physical principle [33,34]. Furthermore, the Chinese industry standard JB/T 14073-2022 formally defines the "heat transfer performance index per unit pump power" as the standardized method for evaluating plate heat exchangers [35].

In this equation, the coefficient 0.5 represents the average of the heat transfer rates on the cold and hot sides. Based on the First Law of Thermodynamics, under ideal steady-state operating conditions and neglecting heat losses, the heat released by the hot fluid per unit time should equal that absorbed by the cold fluid, i.e., $Q_h = Q_c$. Under these conditions, taking the average of the two values is numerically equivalent to using either side's value. This averaging approach reduces the influence of calculation errors on one side and simultaneously adheres to the fundamental principle of energy conservation, providing a more comprehensive assessment of the overall system performance.

In summary, this study investigates the influence of rotary GGH operating parameters on the OSP index. A three-factor, three-level Box-Behnken design is employed to define the computational conditions [36]. This design accommodates 3 to 7 factors; for k factors, the number of required experiments is given by $N = 2k(k-1) + C$, where C denotes the number of central points. Typically, 15 to 62 experimental runs are sufficient. When optimizing multiple factors, the Box-Behnken design allows a relatively small number of experimental schemes to generate a dataset suitable for subsequent analysis.

The factor levels used in this study are listed in Table 4: rotational speed A = 0.1–1 rpm, treated gas inlet temperature B = 180°C–250°C, and inlet velocity C = 8–12 m/s. The experimental design comprises 12 distinct combinations of the independent variables plus 3 central point combinations, resulting in a total of 15 operating conditions.

Table 4: The ranges of each factor in response surface design.

Level	Factor *A*	Factor *B*	Factor *C*
−1	0.1	180	8
0	0.55	215	10
1	1	250	12

4 Results and Analysis

4.1 Simulation Results and Variance Analysis

Table 5 lists the 15 operating conditions and their corresponding response values obtained from numerical simulation, while Table 6 summarizes the results of the variance analysis.

Table 5: Box-Behnken experimental design and response values.

Serial Number	Factor *A*	Factor *B*	Factor *C*	Response Value Y
1	0.55	215	10	76.982
2	0.55	215	10	76.982
3	0.55	180	8	63.276
4	0.1	250	10	93.173
5	0.1	215	12	62.017
6	1	250	10	99.508
7	0.55	215	10	76.982
8	0.55	180	12	48.499
9	1	215	12	66.025
10	0.55	250	8	104.983
11	0.1	180	10	54.279
12	0.1	215	8	81.214
13	1	215	8	85.681
14	1	180	10	57.384
15	0.55	250	12	84.718

Table 6: Results of the analysis of variance.

Source	Degree of Freedom	AdjSS	AdjMS	*F*-Value	*p*-Value
Model	9	3911.26	434.58	695.16	0.000
Linear	3	3880.62	1293.54	2069.13	0.000
Square	3	20.46	6.82	10.91	0.012
Interaction term	3	10.19	3.40	5.43	0.050
Error	5	3.13	0.63		
Total	14	3914.39			
R^2 = 99.92%	Adj R^2 = 99.78%	Pred R^2 = 98.72%			

As shown in the table, the coefficient of determination (R^2) for the regression equation is 99.92%, indicating an excellent model fit. The adjusted R^2 and predicted R^2 values are also close to 1, further confirming the model's high reliability and predictive capability. Therefore, the model can be considered accurate in representing the relationship between the input factors and the response variable. The quadratic response surface equation is presented in Eq. (8), and Table 7 lists the regression coefficients for each parameter.

$$Y = 76.98 + 2.24A + 19.87B - 9.24C + 0.8073AB - 0.1148AC - 1.37BC - 1.27A^2 + 0.3693B^2 - 1.98C^2 \quad (8)$$

The p-value indicates whether a given factor's effect on the response variable is statistically significant in the presence of other factors in the model. Conventionally, a factor is deemed significant when $p \leq 0.05$; conversely, when $p > 0.05$ suggest an insignificant effect, falling outside the 95% confidence interval [37]. As shown in Table 7, all three selected factors have a significant influence on the OSP performance. Although the p-values for certain interaction terms (AB and AC) exceed 0.05, the Box-Behnken design depends on a full quadratic model, and removing statistically insignificant terms may create a mismatch between the model structure and the experimental design. Table 8 compares model performance before and after removing the AB and AC terms; R^2 decreased from 99.92% to 99.88%, adjusted R^2 decreased from 99.78% to 99.75%, and predicted R^2 decreased from 98.72% to 98.65%. These minor changes indicate no meaningful improvement in predictive capability, and the lack-of-fit test remained non-significant ($p > 0.05$), confirming that retaining these non-significant interaction terms does not induce overfitting. Therefore, the response surface model in this study adheres to the hierarchical principle, which requires that all corresponding first-order terms be retained whenever quadratic or interaction terms are included, preserving both the model's hierarchical integrity and predictive stability.

Table 7: Regression coefficients for overall system performance indicators.

Item	Coefficient	Standard Error of the Coefficient	*T*-Value	*p*-Value
Constant	76.98	0.456	168.64	0.000
A	2.24	0.280	8.01	0.000
B	19.87	0.280	71.07	0.000
C	−9.24	0.280	−33.04	0.000
$A * A$	−1.27	0.411	−3.07	0.028
$B * B$	0.3693	0.411	0.90	0.411
$C * C$	−1.98	0.411	−4.82	0.005
$A * B$	0.8073	0.395	2.04	0.097
$A * C$	−0.1148	0.395	−0.29	0.783
$B * C$	−1.37	0.395	−3.47	0.018

Table 8: Comparison of results from simplified models.

Model	R^2	Adj. R^2	Pred. R^2
Complete model (including items AB and AC)	99.92%	99.78%	98.72%
Simplified model (excluding items AB and AC)	99.88%	99.75%	98.65%

The analysis of the variance results indicates that the *p*-value for the interaction between rotational speed and inlet temperature (A × B) is 0.097, and that for the interaction between rotational speed and inlet velocity (A × C) is 0.783; neither interaction is statistically significant. In contrast, the *p*-value for the interaction between inlet temperature and inlet velocity (B × C) is 0.018, indicating moderate significance. These interactions arise from the inherent coupling mechanisms within the heat transfer process.

Interaction between rotational speed and inlet temperature: Rotational speed determines the contact time between the heat transfer element and the flue gas, whereas inlet temperature controls the driving temperature difference for heat transfer. At high inlet temperatures, the large temperature difference enables effective heat transfer even at lower rotational speeds. Conversely, when the inlet temperature is low, increasing the rotational speed becomes necessary to offset the reduced temperature gradient. Consequently, rotational speed and inlet temperature exhibit a complementary effect on OSP, reflected by a positive interaction coefficient (+0.8073).

Interaction between inlet temperature and inlet velocity: Inlet temperature influences the physical properties of the flue gas—particularly density and viscosity—while inlet velocity governs the flow regime. Increased temperature reduces gas density and increases viscosity, thereby modifying the interplay between velocity, pressure drop, and heat transfer. For example, at high temperatures, the reduced density alleviates the pressure drop typically induced by higher velocities, partially counteracting the adverse effect of increased velocity on OSP. This interaction is reflected by a significant negative coefficient (–1.37).

Interaction between rotational speed and inlet velocity: This interaction is not significant. Rotational speed primarily determines the contact duration between the heat transfer element and flue gas, whereas inlet velocity predominantly influences the convective heat transfer coefficient and flow resistance. Because these factors affect OSP through largely independent mechanisms that operate at different stages of the heat transfer process, their interaction is statistically negligible. This finding aligns with physical expectations and further supports the validity of the model.

4.2 Response Surface Analysis

In this study, Design-Expert software was employed to analyze the response data. Fig. 6 illustrates the response surface of the rotary GGH OSP under the interactive effects of the study factors [38].

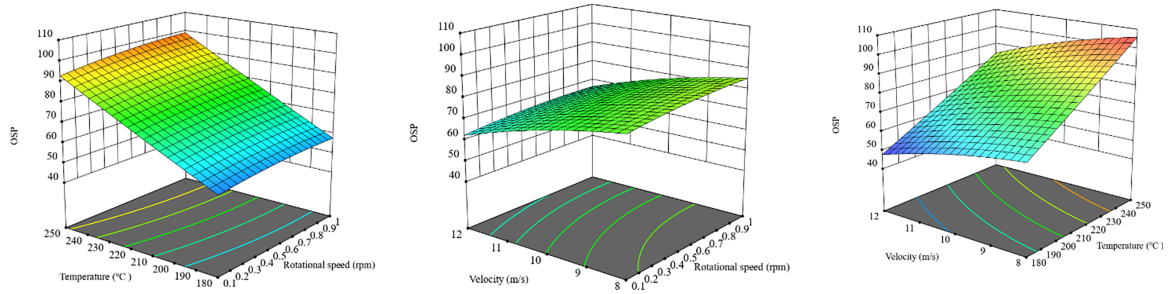

(a) (b) (c)

Figure 6: Response surface plot of the overall system performance indicators of the rotary GGH under the interactive influences of different factors: (**a**) Interaction of rotational speed and inlet temperature; (**b**) Interaction of rotational speed and inlet velocity; (**c**) Interaction of inlet temperature and inlet velocity.

As shown in Fig. 6a, at a constant velocity, the OSP index of the rotary GGH increases with increasing rotational speed, though the rate of increase gradually diminishes and eventually plateaus near 1 rpm. This behavior stems from the periodic heat storage and the release of the heat exchange elements: as the

rotary GGH rotates, these elements alternately traverse the high-temperature untreated flue gas and the low-temperature purified flue gas, completing a cylindrical "heat storage-heat release" process. Higher rotational speeds increase the number of thermal cycles per unit time, promoting a more uniform temperature distribution on both the hot and cold sides and enhancing heat transfer efficiency. However, beyond a certain speed, the residence time on each side becomes insignificant for complete heat transfer before transitioning to the opposite side, showing further efficiency improvement. This trend aligns with the findings of Özdemir & Serincan, who identified a "critical rotational speed" beyond which performance improvements in rotary heat exchangers plateau.

As shown in Fig. 6b, at a constant temperature, the OSP decreases with increasing inlet velocity due to the trade-off between enhanced heat transfer and increased flow resistance. Convective heat transfer principles dictate that the Nusselt number ($Nu = hD/\lambda$) increases with the Reynolds number ($Re = \rho uD/\mu$), following $Nu \propto Re^n$ ($n \approx 0.6$–0.8). Higher inlet velocities increase Re, thereby increasing Nu and the convective heat transfer coefficient h, which boosts the heat transfer rate Q. However, flow resistance grows more sharply with velocity: in porous media, the Darcy-Forchheimer equation predicts the pressure drop as $\Delta P = au + bu2$, causing the total pumping power PP_t to rise far faster than Q [39]. For example, increasing velocity from 8 to 12 m/s increases Q by only 15%–20%, whereas PP_t surges by 60%–80%, substantially reducing OSP. This demonstrates the presence of an optimal velocity range, beyond which additional energy input yields diminishing heat transfer gains [40].

As shown in Fig. 6c, the OSP index of the rotary GGH increases with increasing net flue gas inlet temperature. This behavior results from two interrelated mechanisms. First, higher inlet temperatures increase the temperature difference between the hot and cold flue gas streams, strengthening the heat transfer driving force. Second, temperature-dependent changes in flue gas properties affect flow resistance: as temperature rises, gas density decreases while viscosity increases. Since the pressure drop scales with density ($\Delta P \propto \rho u^2$), the reduced density lowers the pressure drop, slightly decreasing pumping power PP_t. Consequently, the combined effect of enhanced heat transfer and reduced energy consumption thus produces a significant increase in OSP.

Based on the response surface plot of OSP, an optimal combination of operating conditions exists within the studied parameter ranges that maximizes system performance. Using a response optimizer to target energy efficiency and reduced consumption, this optimal parameter set is identified, as shown in Fig. 7.

Optimization		Rotational Speed/rpm	Temperature/°C	Velocity/m/s
D	High	1.0	250	12
1.000	Current	1.0	250	8
	Low	0.1	180	8
OSP Max value 107.7425				

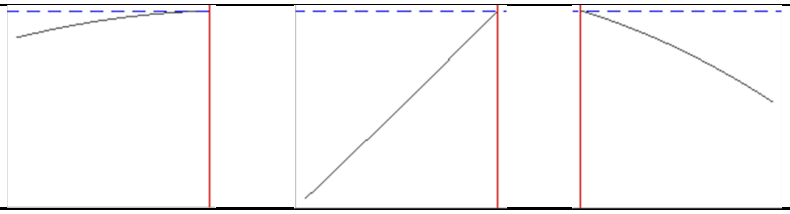

Figure 7: Optimization values of each parameter response.

The comprehensive fitness index (D) quantifies how effectively a combination of factors meets the response objective, with $D = 1$ representing the ideal scenario. Within the studied variable ranges, the optimal operating conditions are a rotational speed of 1 rpm, a post-treatment flue gas inlet temperature of 250°C,

and an inlet velocity of 8 m/s. Under these settings, the predicted OSP index reaches 107.7425. Notably, this optimal solution occurs at the upper limits of temperature and rotational speed and the lower limit of inlet velocity, indicating that the performance is maximized at the safety boundaries. Further temperature increases would exceed the thermal limits of the SCR catalyst, reductions in inlet velocity would raise the risk of ash deposition, and higher rotational speed would produce diminishing returns while increasing leakage risk. These results confirm that the identified optimal parameters achieve the best performance attainable under the imposed safety constraints, demonstrating the effectiveness of the constraint-integrated optimization approach.

5 Conclusion

This study examines the rotary GGH employed in low- and medium-temperature denitrification systems for cement kiln flue gas. By integrating CFD with the RSM, the effects of key operating parameters—including treated flue gas inlet temperature, inlet velocity, and rotor speed—on the overall GGH performance are systematically evaluated. The OSP index, which balances heat transfer rate against pumping power, is adopted as the optimization criterion to determine the optimal combination of the operating conditions. The principal conclusions are summarized as follows:

(1) A full-scale numerical framework for rotary GGHs, formulated using the LTNE porous media model in conjunction with the Multiple Reference Frame (MRF) approach, reasonably produces the coupled flow and heat transfer behavior within the heat exchanger. Validation against analytical solutions reported in the literature demonstrates strong agreement, with relative errors for all evaluated parameters remaining below 5%, which supports the reasonable accuracy and predictive capability of the model within the scope of the present study. The proposed OSP index, defined as the ratio of heat transfer rate to pumping power, provides a practically useful engineering metric reconciling the inherent trade-off between heat transfer performance and energy consumption. This index offers clear interpretability and is suitable for the engineering optimization of operating parameters.

(2) The influence of operating parameters on the OSP index can be summarized as follows. At a constant inlet velocity, OSP increases with increasing rotor speed; however, the incremental gain progressively diminishes, with performance approaching saturation beyond approximately 1 rpm. Under isothermal conditions, OSP decreases monotonically as the inlet velocity increases. In contrast, when both rotor speed and inlet velocity are held constant, OSP exhibits a positive correlation with the treated flue gas inlet temperature.

(3) Response surface analysis demonstrates that all operating parameters exert statistically significant effects on the OSP index, with treated flue gas inlet temperature showing the most pronounced influence. A positive interaction is observed between rotor speed and inlet temperature (coefficient: +0.8073), whereas a negative interaction characterizes the coupling between inlet temperature and inlet velocity (coefficient: −1.37). In contrast, the interaction between rotor speed and inlet velocity is not statistically significant, indicating that their respective influences on OSP operate through largely independent mechanisms.

(4) Under the constraint of ensuring safe system operation, the Box-Behnken design was used to directly incorporate engineering limits into the optimization framework. The resulting optimal operating conditions comprise a treated flue gas inlet temperature of 250°C, an inlet velocity of 8 m/s, and a rotor speed of 1 rpm. It should be emphasized that these optimized operating points are strictly valid only within the imposed parameter ranges and safety constraints. Under this parameter combination,

the OSP attains a maximum value of 107.74, with the optimum located precisely on the safety boundary. This outcome demonstrates the practical applicability of the constraint-integrated optimization strategy for engineering-oriented performance enhancement.

Acknowledgement: Not applicable.

Funding Statement: The authors received no specific funding for this study.

Author Contributions: The authors confirm contribution to the paper as follows: study conception and design: Fuping Qian, Yi Sun, Dong Wang; data collection: Yi Sun, Kaiwen Cheng, Chen Zhu; analysis and interpretation of results: Kaiwen Cheng, Yi Sun, Fuping Qian; draft manuscript preparation: Kaiwen Cheng, Yi Sun. All authors reviewed and approved the final version of the manuscript.

Availability of Data and Materials: The authors confirm that the data supporting the findings of this study are available within the article.

Ethics Approval: Not applicable.

Conflicts of Interest: The authors declare no conflicts of interest.

References

1. Barbhuiya S, Bhusan Das B, Adak D. Roadmap to a net-zero carbon cement sector: strategies, innovations and policy imperatives. J Environ Manag. 2024;359(5):121052. doi:10.1016/j.jenvman.2024.121052.
2. Huang J, Zhao D, Zhao P. Review on technical pathways and assessment for carbon peaking and carbon neutrality in China's building materials industry. Discov Sustain. 2025;6(1):1188. doi:10.1007/s43621-025-02006-x.
3. Xu X, Huang B, Liu L, Cao Z, Gao X, Mao R, et al. Modernizing cement manufacturing in China leads to substantial environmental gains. Commun Earth Environ. 2022;3(1):276. doi:10.1038/s43247-022-00579-3.
4. State Council of the People's Republic of China. Action plan for carbon dioxide peaking before 2030. 2021 [cited 2026 May 7]. Available from: http://english.www.gov.cn/policies/latestreleases/202110/27/content_WS6178a47ec6d0df57f98e3dfb.html.
5. Ministry of Ecology and Environment of the People's Republic of China. Opinions on promoting the implementation of ultra-low emissions in the cement industry. 2024 [cited 2026 May 7]. Available from: https://www.mee.gov.cn/.
6. Li Z, Sun L, Zhang R, Hanaoka T. Decarbonization pathways promote improvements in cement quality and reduce the environmental impact of China's cement industry. Commun Earth Environ. 2024;5(1):769. doi:10.1038/s43247-024-01929-z.
7. Lin D, Zhang L, Liu Z, Wang B, Han Y. Progress of selective catalytic reduction denitrification catalysts at wide temperature in carbon neutralization. Front Chem. 2022;10:946133. doi:10.3389/fchem.2022.946133.
8. Guo Y, Luo L, Zheng Y, Wang J, Zhu T. Low-medium temperature application of selective catalytic reduction denitration in cement flue gas through a pilot plant. Chemosphere. 2021;276:130182. doi:10.1016/j.chemosphere.2021.130182.
9. Dallaire J, Gosselin L, da Silva AK. Conceptual optimization of a rotary heat exchanger with a porous core. Int J Therm Sci. 2010;49(2):454–62. doi:10.1016/j.ijthermalsci.2009.07.027.
10. Alhusseny A, Turan A. An effective engineering computational procedure to analyse and design rotary regenerators using a porous media approach. Int J Heat Mass Transf. 2016;95(2):593–605. doi:10.1016/j.ijheatmasstransfer.2015.12.033.
11. Güllüce H, Özdemir K. Design and operational condition optimization of a rotary regenerative heat exchanger. Appl Therm Eng. 2020;177:115341. doi:10.1016/j.applthermaleng.2020.115341.
12. Ghodsipour N, Sadrameli M. Experimental and sensitivity analysis of a rotary air preheater for the flue gas heat recovery. Appl Therm Eng. 2003;23(5):571–80. doi:10.1016/S1359-4311(02)00226-0.

13. Wang H, Han C. Research on SCR denitrification technology for cement kiln flue gas. Energy Sci Technol. 2023;21(4):93–6. (In Chinese).
14. Han Y, Sun Y, Wu J. A low-cost and efficient solar/coal hybrid power generation mode: integration of non-concentrating solar energy and air preheating process. Energy. 2021;235(5):121367. doi:10.1016/j.energy.2021.121367.
15. Qin Y, Cai W, Li Z, Li G, Liu P, An B, et al. Ce doped V-W/Ti as selective catalytic reduction catalysts for cement kiln flue gas denitration. Environ Sci Pollut Res. 2024;31(2):2053–66. doi:10.1007/s11356-023-31165-5.
16. Li J, Sun P, Cheng X, Li X, Bi XT, Wang Z, et al. A novel integrated rotary reactor for NO reduction by CO and air preheating: reactor design and heat transfer modelling. Appl Therm Eng. 2021;190:116815. doi:10.1016/j.applthermaleng.2021.116815.
17. Zmrhal V, Kučera M. The effect of leakage on pressure loss of rotary regenerative heat exchangers. Int J Refrig. 2023;154:364–77. doi:10.1016/j.ijrefrig.2023.07.004.
18. Jiang K, Zhang G, Liu H, Mu Z, Wang Q, Qin T, et al. Design and dynamic simulation of flue gas-molten salt heat exchanger in flexible operation coal-fired power plant. J Energy Storage. 2024;93(9):112227. doi:10.1016/j.est.2024.112227.
19. Dhumal GS, Havaldar SN. Enhancing heat transfer performance in a double tube heat exchanger: experimental study with twisted and helical tapes. Case Stud Therm Eng. 2023;51(5):103613. doi:10.1016/j.csite.2023.103613.
20. Kanaś P, Jedlikowski A, Anisimov S. The influence of geometrical parameters on heat and mass transfer processes in rotary heat exchangers. SN Appl Sci. 2019;1(6):526. doi:10.1007/s42452-019-0540-2.
21. Manaswini R, Manjunatha S, Chamkha AJ, Tanuja TN. A comparative heat transfer analysis of rectangular fin through LTE and LTNE model. Eur Phys J Plus. 2025;140(8):787. doi:10.1140/epjp/s13360-025-06711-4.
22. Ali RMK, Lafta Ghashim S. Numerical analysis of the heat transfer enhancement by using metal foam. Case Stud Therm Eng. 2023;49(11):103336. doi:10.1016/j.csite.2023.103336.
23. Shashi Prabha GS, Bharathi MC, Kudenatti RB. Heat transfer through mixed convection boundary layer in a porous medium: LTNE analysis. Appl Therm Eng. 2020;179(4):115705. doi:10.1016/j.applthermaleng.2020.115705.
24. Zhu C, Ma X, Chen L, Ma Q, Sun Y, Qian F. Porous media-based full-scale modeling of thermal behavior in rotary gas-gas heat exchangers. Fluid Dyn Mater Process. 2025;21(8):1895–915. doi:10.32604/fdmp.2025.067899.
25. Shi C, Cai J, Ren Q, Wu H. Optimization of fuel *in-situ* reduction (FISR) denitrification technology for cement kiln using CFD method. J Therm Sci. 2023;32(6):2256–72. doi:10.1007/s11630-023-1720-3.
26. Močnik U, Čikić A, Muhič S. Numerical and experimental analysis of fluid flow and flow visualization at low Reynolds numbers in a dimple pattern plate heat exchanger. Energy. 2024;288:129812. doi:10.1016/j.energy.2023.129812.
27. Giunti L, Giacomelli F, Močnik U, Villi G, Milazzo A, Talluri L. Numerical analysis of pressure drops in single-phase flow through channels of brazed plate heat exchangers with dimpled corrugated plates. Appl Sci. 2025;15(15):8431. doi:10.3390/app15158431.
28. Shawish S, Mostafa CB, Al-Waked RF, Nasif MS. CFD simulation of energy transfer within a membrane heat exchanger under turbulent flow. Jordan J Mech Ind Eng. 2023;17(2):139–54. doi:10.59038/jjmie/170201.
29. Soleimanikutanaei S, Lin CX, Wang D. Numerical modeling and analysis of transport membrane condensers for waste heat and water recovery from flue gas. Int J Therm Sci. 2019;136(3):96–106. doi:10.1016/j.ijthermalsci.2018.10.014.
30. Özdemir K, Serincan MF. A computational fluid dynamics model of a rotary regenerative heat exchanger in a flue gas desulfurization system. Appl Therm Eng. 2018;143(1):988–1002. doi:10.1016/j.applthermaleng.2018.08.011.
31. Wejkowski R, Wojnar W. Selective catalytic reduction in a rotary air heater (RAH-SCR). Energy. 2018;145(5):367–73. doi:10.1016/j.energy.2017.12.077.
32. Rincón Tabares JS, Perdomo-Hurtado L, Aragón JL. Study of gasketed-plate heat exchanger performance based on energy efficiency indexes. Appl Therm Eng. 2019;159(14):113902. doi:10.1016/j.applthermaleng.2019.113902.
33. Qasem NAA, Al-Ghamdi AA, Zubair SM. An assessment of optimal airside heat transfer per unit friction power characteristics of compact heat exchangers. Int J Refrig. 2019;99:479–89. doi:10.1016/j.ijrefrig.2018.12.030.
34. Boraey MA. An energy-utilization metric for heat transfer devices. Prog Nucl Energy. 2021;142(1):104006. doi:10.1016/j.pnucene.2021.104006.

35. JB/T 14073-2022. Performance and evaluation method for plate heat exchanger in air conditioning and heat pump systems. Beijing, China: Ministry of Industry and Information Technology of the People's Republic of China; 2022.
36. Ferhi M, Mliki B, Miri R, Djebali R. Optimization of co-flow micro-heat-exchanger performance using response surface methodology: energy transfer rate and thermodynamic irreversibility. FME Trans. 2025;53(3):409–25. doi:10.5937/fme2503409f.
37. Glazar V, Trp A, Lenic K. Optimization of air-water microchannel heat exchanger using response surface methodology. Int J Heat Mass Transf. 2020;157(13):119887. doi:10.1016/j.ijheatmasstransfer.2020.119887.
38. Mohapatra T, Sahoo SS, Padhi BN. Analysis, prediction and multi-response optimization of heat transfer characteristics of a three fluid heat exchanger using response surface methodology and desirability function approach. Appl Therm Eng. 2019;151(10):536–55. doi:10.1016/j.applthermaleng.2019.02.001.
39. Taler D. Simple power-type heat transfer correlations for turbulent pipe flow in tubes. J Therm Sci. 2017;26(4):339–48. doi:10.1007/s11630-017-0947-2.
40. Azman A, Yusoff MZ, Mukhtar A, Gunnasegaran P, Ching NK, Yasir ASHM. Application of box-behnken design with response surface methodology to analyse friction characteristics for corrugated pipe via CFD. CFD Lett. 2023;15(7):1–13. doi:10.37934/cfdl.15.7.113.